Metrol. Meas. Syst., Vol. 24 (2017), No. 4, pp. 653–674.

PAN POLSKA AKADEMIA NAUK

METROLOGY AND MEASUREMENT SYSTEMS

Index 330930, ISSN 0860-8229

www.metrology.pg.gda.pl

M&MS

ANALYSIS OF FREE-SPACE OPTICS DEVELOPMENT

Janusz Mikołajczyk[1)], Zbigniew Bielecki[1)], Maciej Bugajski[2)], Józef Piotrowski[3)], Jacek Wojtas[1)], Waldemar Gawron[3)], Dariusz Szabra[1)], Artur Prokopiuk[1)]

1) Military University of Technology, Institute of Optoelectronics, Gen. S. Kaliskiego 2, 00-908 Warsaw, Poland (janusz.mikolajczyk@wat.edu.pl, zbigniew.bielecki@wat.edu.pl, jacek.wojtas@wat.edu.pl, dariusz.szabra@wat.edu.pl, ✉ artur.prokopiuk@wat.edu.pl, +48 26 183 7740)

2) Institute of Electron Technology, Al. Lotnikow 32/46, 02-668 Warsaw, Poland (bugajski@ite.waw.pl)

3) VIGO System S.A., Poznańska 129/133, 05-850 Ożarow Mazowiecki, Poland (jpiotr@vigo.com.pl, wgawron@vigo.com.pl)

Abstract

The article presents state of work in technology of free-space optical communications (*Free Space Optics* – FSO). Both commercially available optical data links and their further development are described. The main elements and operation limiting factors of FSO systems have been identified. Additionally, analyses of FSO/RF hybrid systems application are included. The main aspects of *LasBITer* project related to such hybrid technology for security and defence applications are presented.

Keywords: optical communications, open path laser communications, line of sight communications, free space optics.

1. Introduction

During last decades FSO systems became an important direction of optoelectronic technology applications. FSO is also known as fibreless photonics. To obtain a broadband communication channel, *high frequency* (HF) modulated light pulses are used to transmit data through the atmosphere. These systems have been installed in terrestrial systems, as well as in systems for data transmission between space-space, space-earth and marine objects (Fig. 1). Operating in the infrared radiation spectrum, the FSO can provide links with a very high data rate (tens of Gigabits per second) between various platforms offering ranges of several kilometres near the sea level or even over 100 km at high altitude.

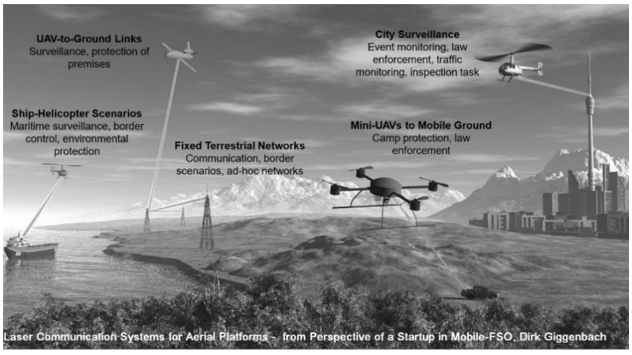

Fig. 1. Examples of scenarios of the FSO systems application.

Article history: received on Jun. 14, 2017; accepted on Sep. 02, 2017; available online on Dec. 01, 2017; DOI: 10.1515/mms-2017-0060.

Important FSO systems' applications are *e.g.*: ad-hoc mobile communications during crisis situations, so-called "last mile" links in urban areas, a special data transfer *e.g.* between ships and land, and secret military data links. It was shown that a command centre would be able to send information to vehicles or soldiers at a distance of "line-of-sight" with a transmission rate from 25 Mbps to 1.25 Gbps [1].

The most important advantages of FSO technology are:

- use of radiation spectra is not covered by formal regulation;
- high transmission rates up to 10 Gbps [2];
- no interferences with other transmissions (insensitivity to EM interference);
- fast, low-cost and easy installation;
- high immunity to interception and jamming;
- user-adjusted capacity with an option of data link reconfiguration;
- commercial availability.

The main disadvantage of the FSO system is its high sensitivity on weather conditions (atmospheric attenuations). Different weather phenomena like fog, snow and rain, turbulence, are able to scatter and to absorb the optical signal. As a result, both range and data rate of data transmission channel are reduced. To minimize the influence of these negative factors, characterization of various weather conditions and selection of so-called atmosphere transmission windows are required [3]. The recent developments in optoelectronic technology make it possible to construct some FSO systems alternative to RF wireless ones in mainstream communication applications.

The paper is arranged as follows. In Section 2, the fundamental knowledge of FSO system construction is given. The influence of selected atmospheric effects and other factors on FSO link performance is analysed in Sections 3 and 4. A description related to the selection of a radiation wavelength for FSO communication is included in Section 5. The research results of the FSO systems designed at the Institute of Optoelectronics, MUT are presented in Sections 6, 7 and 8, together with a concept of FSO/RF hybrid system based on the "LaserBITer" project, financed by the Polish National Centre of Research and Development .

2. Free Space Optics

In general, an FSO link consists of an optical signal transmitter and a receiver. As shown in Fig. 2, the transmitter is used to transmit data signals in free space by modulation of optical radiation. Its main elements are a radiation source, a laser modulator and optical devices.

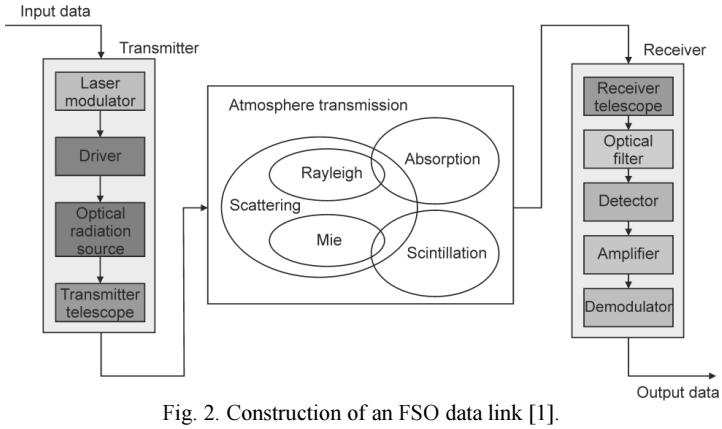

Fig. 2. Construction of an FSO data link [1].

The laser modulator modulates the optical signal with an electrical one by varying *e.g.* the laser biasing current. The most popular optical device is a telescope. It is applied to direct optical radiation towards the receiver.

The optical signal is attenuated in the atmosphere by absorption, scattering, scintillation, propagation geometrics and other phenomena. In practice, the total radiation attenuation $A(\lambda)$ caused by atmosphere can be calculated as:

$$A(\lambda) = \alpha_{\text{fog}}(\lambda) + \alpha_{\text{snow}}(\lambda) + \alpha_{\text{rain}}(\lambda) + \alpha_{\text{scattering}}(\lambda), \text{ [dB/km]}, \quad (1)$$

where $\alpha_x(\lambda)$ is attenuation caused by the mentioned weather conditions and λ is an operational wavelength.

The receiver usually consists of a telescope, an optical filter, a photodetector, a preamplifier (preamp), and a demodulator for proper retrieving the information signal. The telescope collects and focuses the optical radiation on the photodetector active area. The filter reduces the background radiation (*e.g.* solar illumination). The photodetector converts the photon energy into an electrical signal. It should provide a high responsivity at the wavelength of interest, a small value of noise, sufficient values of dynamic range and signal bandwidth. The most commonly used photodetectors are a pin photodiode and an *avalanche photodiode* (APD). The photodetector output signal is amplified by a special construction of preamp. During the last procedure, the amplified signal is analysed using the demodulator.

To determine performance of FSO link, many factors should be taken into account, *e.g.* the operation wavelength, the light source power, the beam divergence angle, the photodetector detectivity and the aperture diameters of applied optical devices.

The beam size at the receiver surface is dependent on the beam divergence and the transmission range. Typically, the beam divergence is used in a range from 1 mrad to 8 mrad, although in some special links the values from 6 μrad up to 180° are also applied [5, 6].

The selection of a light source for FSO applications depends on various factors. The most important are: the radiation pulse power, modulation capabilities, lifetime, eye safety, beam size and divergence angle, physical dimensions, compatibility with other transmission media, price and purchase availability. The parameter values of some radiation sources applied in selected FSO systems are listed in Table 1.

Table 1. Light sources applied in selected FSO systems.

Laser	Wavelength [nm]	Laser/LED power	Beam divergence	Application	Data source
Matrics LEDs	450	6 W	180°	Underwater communication	www.sonardyne.com
Nd:YAG	532	250 mJ 12 ns	110 μrad	Deep space mission	[7]
LD	532/486	5 W	180°	Underwater communication	www.saphotonics.com
LD	785	25 mW	1 mrad	Ethernet	www.geodesy-fso.com
AlGaAs	830	60 mW	6 μrad	Inter-satellite communication	[5]
Argon-ion/GaAs	830	13 W	20 μrad	Ground-to-satellite link	[8]
VCSEL	850	9 mW	3.5 mrad	Last mile link	www.polixel.pl
LED	800–900	bd	17 mrad	Communication between buildings	freespaceoptics.ca
LD	1550	113 mW	50 mrad	UAV-to-UAV link, L = 2km	[9]
LD	1550	200 mW	19.5 μrad	Ground-to-UAV link	[10]
QCL	8400	740 mW (100ns, f = 1 MHz)	2 mrad	Laboratory FSO link (IOE MUT)	[11]

Laser diodes (LDs) are typically used in current commercially available FSO systems. However, in some FSO constructions non-lasing sources such as *light-emitting diodes* (LEDs) or *IR-emitting diodes* (IREDs) are also applied. But – compared with LEDs – LDs are characterized by a higher output power, energy efficiency, modulation rate, and by a less diverged beam. Laser diodes called *vertical emitting lasers* (VCSELs) are high-speed radiation sources that ideally suit for high-speed (Gbps) data communication. These lasers are also characterized by very low threshold currents, non-stringent requirements for the modulation signal, and a good beam quality. They are relatively stable and therefore do not require power control using a photodiode monitor. The most common VCSELs are composed of GaAs/AlGaAs to emit light in a range of 750–980 nm.

Recently, *quantum cascade lasers* (QCLs) are used as infrared radiation sources ($\lambda \sim 3.5 \div 24$ μm) basing on the unipolar lasing mechanism; QCLs have unique high-frequency characteristics with theoretical bandwidths above 100 GHz [12].

In addition, there has been also developed a high-bandwidth underwater communication system using blue-green lasers. For example, the BlueComm modem family constructed by Sonardyne company provides data transmission rates exceeding 500 Mbps. A transmission rate of 1 Gbps at distances greater than 150 m was also reported [13].

In practice, there are four common topologies of FSO networks: point-to-point, point-to-multipoint, mesh, and ring ones. However, these topologies can be combined. In the point-to-point arrangement, a transmission rate from 155 Mbps to 10 Gbps at a distance from 2 km to 4 km can be obtained. Such a link provides a dedicated connection with a higher bandwidth, but it is not cost-effectively. In comparison, the point-to-multipoint configuration is cheaper but offers a worse bandwidth (the same data rate at a distance from 1 km to 2 km). The mesh topology is able to transmit data with a rate of 622 Mbps at shorter distances from 200 m to 450 m. The ring topology is usually used in metropolitan networks. There are "backbones" represented by fibre or FSO high-speed rings [14].

A roadmap of FSO technology is shown in Fig. 3. It can be noticed that since 1990s there have been commercially available FSO systems with data rates of up to several tens of Mbps. Nowadays, this rate has been gradually increasing up to 10 Gbps.

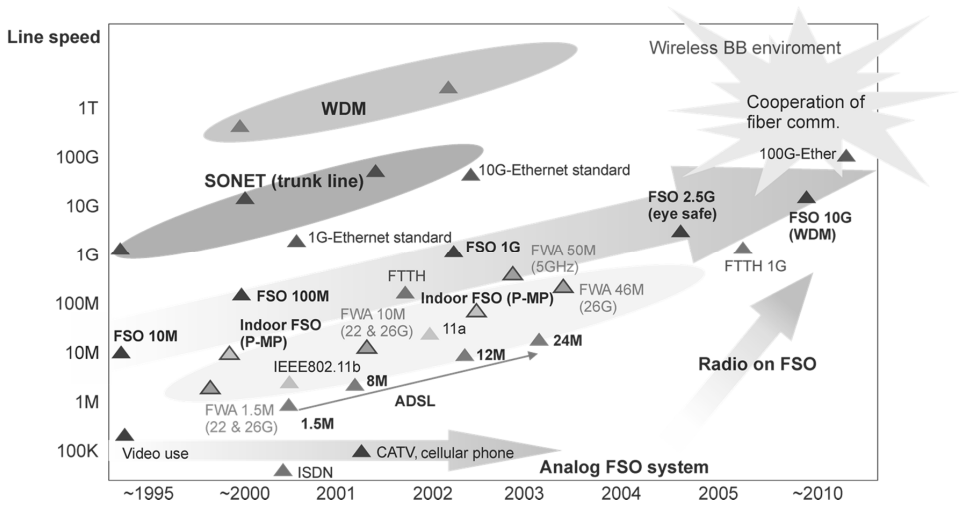

Fig. 3. A roadmap of FSO technology [15].

3. Atmospheric effects

The atmosphere interactions with optical radiation due some phenomena depend on its composition. Practically, the atmosphere consists of different molecular species and small particles like aerosols (fog, forest exudates, dust, sea-salt particles, soil particles, volcano debris, particulate, air pollutants, smog and smoke), ice particles, and water droplets. Thus, the atmosphere causes attenuation of optical signals by absorption, scattering, and scintillation. Nonetheless, atmospheric transmission windows are defined by the molecular absorption, that is a spectral selective phenomenon (Fig. 4) [16]. In general, an atmospheric attenuation τ is described by Beer's law:

$$\tau = exp\left[-\left(\alpha_{abs} + \beta_{scat}\right)L\right], \tag{2}$$

where: L is a distance between the transmitter and receiver; α_{abs} and β_{scat} are coefficients of atmosphere absorption and scattering, respectively.

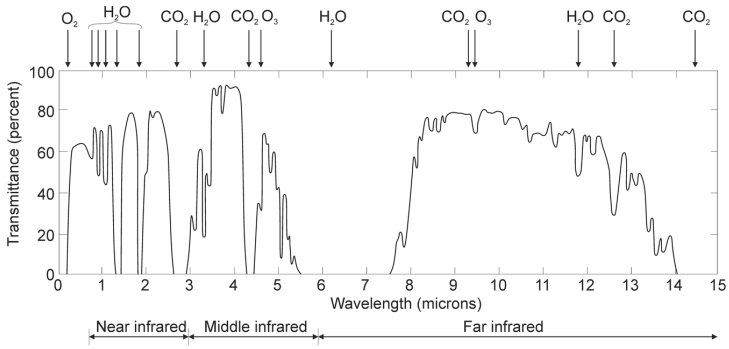

Fig. 4. Transmittance through the atmosphere as a function of wavelength.

Absorption is caused by atmospheric molecules, the energy levels of which can be excited by incident photons. An absorption coefficient depends on the type, effective absorption cross-section σ_{abs} and concentration N_{abs} of gas molecules. These parameters are related as follows [17]:

$$\alpha_{abs} = \sigma_{abs} N_{abs}. \tag{3}$$

The scattering process causes propagation of the redirected radiation beam propagates in various directions different from the original one [2]. There are three main types of scattering: Rayleigh, Mie, and non-selective. The scattering type depends on the relationship between the size of scattering particles and the wavelength of propagated light. *Rayleigh scattering* is caused by particles with a size much smaller than the light wavelength. In this case, the scattering intensity decreases with the wavelength as $\sim\lambda^{-4}$. When the particle size is comparable with or is as large as the radiation wavelength, *Mie scattering* is observed. *Non-selective scattering* occurs for particles' sizes greater than the beam wavelength. In this case, the Mie theory is approximated by the principles of reflection, refraction and diffraction. The scattering coefficient depends on the concentration N_{scat} and effective cross-section σ_{scat} parameter values of the particles and can be described by:

$$\beta_{scat} = \sigma_{scat} N_{scat}. \tag{4}$$

The total scattering coefficient is given by:

$$\beta_{scat} = \beta_m + \beta_a, \tag{5}$$

where β_m and β_a denote Rayleigh (molecular) and Mie (aerosols) scattering.

The Rayleigh scattering coefficient is given by:

$$\beta_m = \sigma_m N_m, \tag{6}$$

where: σ_m is a Rayleigh scattering cross-section; N_m is a volumetric density of air molecules.

The parameter σ_m depends on the index of refraction n, volumetric density of the molecules N, and the radiation wavelength:

$$\sigma_m = \frac{8\pi^3\left(n^2-1\right)^2}{3N^2\lambda^4}. \tag{7}$$

Rayleigh scattering is significant in the ultraviolet and visible spectral ranges. Moreover, it is negligible in the infrared range. The Mie scattering coefficient is expressed by:

$$\beta_a = \sigma_a N_a, \tag{8}$$

where: σ_a is a Mie scattering cross-section; and N_a is a volumetric density of air particles.

The value of coefficient β_a can be estimated by visibility V with the expression[1]:

$$\beta_a = \left(\frac{3.91}{V}\right)\left(\frac{0.55}{\lambda}\right)^{\delta}, \tag{9}$$

where: δ is a coefficient with a value between 0.7 and 1.6 corresponding to visibility conditions given in km; λ is a wavelength of propagating beam (μm) [19].

The fog particles float in the air for a longer time than rain droplets. Additionally, they are characterized by a size smaller than the radiation wavelength. Thus, the scattering due to rainfall (non-selective scattering) is less effective than to fog (Mie scattering). The rain scattering coefficient can be determined using the Stroke Law [20]:

$$\beta_{rain\ scat} = \pi r^2 N_a Q_{scat}\left(\frac{r}{\lambda}\right), \tag{10}$$

where: r is a radius of raindrop (from 0.001 cm to 0.1 cm); N_a is a distribution of rain drops, and Q_{scat} is a scattering efficiency.

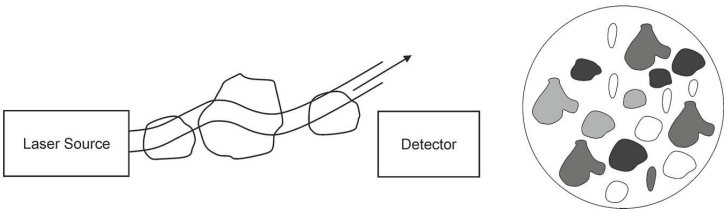

Fig. 5. Optical path changes due to turbulence: eddies are larger than the beam diameter, with scintillation spots and aperture averaged.

Another important atmospheric factor that limits FSO data link capabilities is turbulence. *Clear-air turbulence* (CAT) is defined as chaotic streams and eddies of air masses during the absence of any clouds. Such air movements are described as turbulent ones, because air masses are moving at widely different speeds [21]. As a result of this phenomenon phase shifts of the propagated optical radiation are noticed. The distortions of front-wave can be observed as intensity changes referred as scintillation. Aerosols, moisture, temperature and pressure

[1] According to the Kruse model, visibility is defined as a path length, where radiation of 550 nm is attenuated to 0.02 of its original value and it is estimated through observation.

fluctuations produce variations of the air density and thus also its refractive index [3]. Air eddies can bend the optical path if their size is larger than the beam diameter (Fig. 5). In the opposite situation, constructive and destructive interferences are created, resulting in temporal fluctuations of light intensity (spots) at the receiver surface.

For scintillation scaling, a *refractive index structure parameter* C_n^2 is introduced into calculations. A number of parametric models have been formulated to describe the C_n^2 profile. One of the most commonly used model is described by Hufnagel-Valley [23]:

$$C_n^2(h) = 0.00594\left(\frac{v}{27}\right)^2 (10^{-5}h)^{10} exp\left(-\frac{h}{1000}\right) + 2.7\cdot 10^{-16} exp\left(-\frac{h}{1500}\right) + A_0 exp\left(-\frac{h}{100}\right), \tag{11}$$

where: h is an altitude in m; v is a wind speed at high altitude in m/s; A_0 is a turbulence strength on the ground level; $A_0 = 1.7\cdot 10^{-14}\text{m}^{-2/3}$. In practice, this parameter depends also on the geographical location and time of day. There are three different turbulence effects: *scintillation, beam wander* and *beam spreading*. *Scintillation* is the most important for FSO links, causing intensity fluctuations at the receiver surface. The level of scintillation can be measured in terms of the irradiance variance given by:

$$\sigma_i^2 = 1.23 C_n^2 k^{\frac{7}{6}} L^{\frac{11}{6}}, \tag{12}$$

where $k = 2\pi/\lambda$ is the wave number.

The variance is linearly proportional to C_n^2, nearly proportional to both $1/\lambda$ and the square of the link distance [24]. Therefore, systems of shorter wavelengths have a proportionally higher variance caused by scintillations. This effect increases with the data range and becomes more critical for small aperture photo-receivers [25].

Beam wandering, as well as the scintillation index, is an important characteristic of radiation propagation. It determines requirements for tracking and pointing instruments of FSO system [26]. This effect is observed as a random movement of the focused beam on the photodetector surface. The beam wandering is also expressed in terms of local fluctuations of the irradiance intensity. It results in an increase of system *bit error rate* (BER) and, appropriately, the tracking error. Recently, many studies indicated that partly coherent beams are less affected by the turbulence than the fully coherent beams. So, the use of a partly coherent beam source reduces the radiation intensity fluctuation at the receiver [27].

Beam spreading is related to the broadening of the beam size at the receiver surface beyond an expected pure diffraction limit. Fig. 6 shows the laser beam propagation through the turbulent atmosphere.

The additional laser beam spreading caused by turbulence grows with the increase of both refractive index structure parameter C_n and propagation length (Fig. 7). This spreading is expressed as:

$$T_{beam} = 1.33\sigma_I^2 \Gamma^{5/6}, \tag{13}$$

while Γ is given by:

$$\Gamma = \frac{2\lambda L}{2\pi\omega^2(l)}, \tag{14}$$

where: L is a distance from the source; $\omega^2(l)$ is an initial beam waist at $L = 0$. The parameter σ_I defined as a beam amplitude or irradiance equals:

$$\sigma_I^2 = 1.23 C_n^2 \left(\frac{2\pi}{\lambda}\right)^{7/6} L^{11/6}. \tag{15}$$

In the latest FSO systems, some techniques are applied to mitigate such atmospheric effects as scintillation or beam wander. These techniques use *e.g. adaptive optics* (AO), diversity techniques, aperture averaging, and fast tracking antennas.

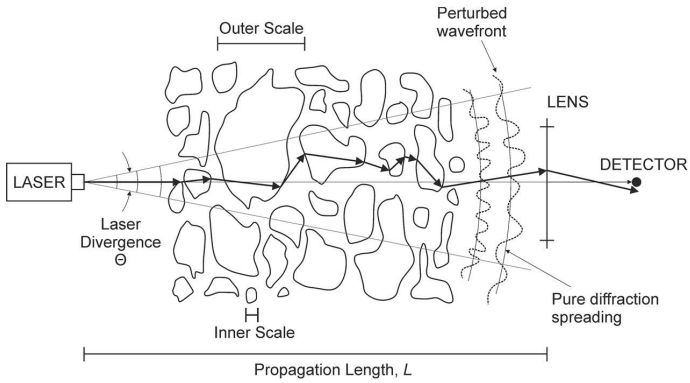

Fig. 6. Propagation of a laser beam through the turbulent atmosphere [28].

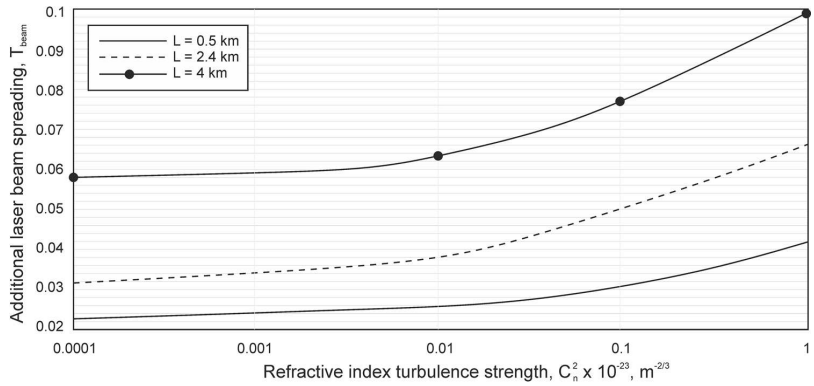

Fig. 7. Laser beam spreading vs. refractive index structure parameter for different propagation lengths and a beam wavelength of 1550 nm [28].

Adaptive optics are designed to continuously measure and correct wave-front errors. Beam diversity can occur in some forms:

- spatial – requiring multiple transmitters and receivers;
- temporal – requiring double transmitted signals, separated by a time delay;
- wavelength – requiring at least two different wavelengths transmission of data.

Numerous methods for fine tracking and automatic acquisition have been developed. These methods include the use of quadrant-detectors, servo-motors, voice-coils, stepping-motors, mirrors, CCD arrays and MEMS [29].

Practical performance of FSO systems is also limited by *geometric losses*. These losses occur when the light beam spreads to a size larger than the receiver's aperture. Geometric loss is expressed by a ratio of the receiver's aperture diameter D_R and irradiated beam diameter D_T. This ratio can be determined by the formula:

$$geometric\ loss = \frac{(D_R)^2}{(D_T + L\theta)^2}, \tag{16}$$

where θ – a beam divergence [mrad]. In general, a system is perfectly aligned when the centre of the Gaussian power distribution is at the optical axis of the receiver.

4. BER, SNR and optical link budget

Taking into account atmospheric attenuation and geometric loss, a radiation power P_R registered by the receiver is given by [30]:

$$P_R = P_T \frac{D_R^2}{(D_R + L\theta)^2} exp(-\tau L), \tag{17}$$

where: P_T is a power emitted by the transmitter; τ is a total coefficient of atmospheric attenuation.

In digital transmission, the BER value is determined as a ratio of the number of bit errors and the total number of transmitted bits during a studied time interval [31]. For FSO communication, it can be described as [32]:

$$BER = \frac{1}{2} erfc\left(\frac{RP_R}{2\sqrt{2N^2}}\right), \tag{18}$$

where: *erfc* is called a Gauss error function; *R* is a detector responsivity; and *N* is thermal noise of the receiver. The value of BER also depends on the modulation scheme. For FSO links with the on-off keying modulation, the BER performance is characterized by a *signal to noise ratio* (SNR) [33]:

$$BER = \frac{exp(-SNR/2)}{(2\pi SNR)^{0.5}}, \tag{19}$$

Taking into account turbulence, the SNR is estimated [22]:

$$SNR = \left(0.31 C_n^2 k^{7/6} I^{11/6}\right)^{-1}, \tag{20}$$

where $I = |E^2|$ is radiation irradiance.

Summarizing, the received optical power can be calculated as [34]:

$$P_R = P_T G_T \eta_T L_{PT} L_{FS} G_R \eta_R L_{PR} L_A, \tag{21}$$

where: η_T, η_R are losses that include imperfect optical components of both transmitter and receiver; $G_T = (\pi D_T/\lambda)^2$ is a gain of the transmitting aperture; $L_{PT} = exp\left(-8\theta_{jit}^2/\theta^2\right)$ is a pointing loss of the transmitter; $L_{FS} = (\lambda/4\pi L)^2$ is a free-space propagation loss; $G_R = (\pi D_R/\lambda)^2$ is a gain of the receiving aperture; L_{PR} is a pointing loss of the receiver; L_A is atmospheric attenuation at the operating wavelength; θ_{jit} is an optical beam jitter angle; and θ is an optical beam divergence as set by diffraction.

It should be also noticed that the application of a high-sensitive photo-receiver in an FSO system with a large-aperture lens makes it possible to increase the influence of the background radiation on the data signal. Sometimes, direct sunlight may cause link outages for a period of time. In these circumstances, narrowing the photo-receiver FOV and using a narrow-bandwidth optical filter can improve the system performance.

5. Wavelength selection for FSO communications

The selection of a wavelength for the FSO data link is a very important issue. Nowadays, commercial FSO systems usually operate in the spectra of 780–850 nm and 1520–1600 nm. To determine a wavelength range, it should be taken into consideration the availability of the main FSO components defined by their transmission range, eye safety, modulation rate, costs, and so on. The eye safety is one of the most important restrictions to the optical power level emitted by an FSO transmitter. Lasers emitting radiation at a wavelength of 1550 nm or about 10000 nm can be used more safely than those with 850 nm and 780 nm. This is due to the fact that infrared

radiation with wavelengths above 1400 nm is absorbed by the transparent parts of the human eye before reaching the retina. That is why the *maximum permissible exposure* (MPE) for these wavelengths is higher than for shorter ones.

The International *Electro-technical Commission* (IEC) classifies lasers into four safety classes depending upon their beam power, wavelength and possible hazards [35]. Most of the FSO systems use Class 1 and Class 1M lasers. For example, an FSO system operating at a wavelength of 1500 nm can transmit a light beam with 50 times higher power comparing with a system working at a shorter wavelength range. It enables to propagate radiation over longer distances in the case of worse weather, and to support higher data rates [30].

In the near-infrared spectrum (NIR, 780÷850 nm), reliable, inexpensive, high-performance optoelectronic devices, *i.e.* lasers and detectors, are readily available and commonly used in the FSO transmission equipment. Advanced VCSEL lasers and silicon photodiodes are used for operation at this wavelength. Si detectors typically have the maximum of their spectral responsivity near the value of 850 nm, making in conjunction with VCSELs very efficient tools. Silicon detectors are ideal for FSO systems operating at a very high bandwidth – 10 Gbps.

The *short-wavelength-infrared spectrum* (SWIR, 1520–1600 nm) is also well applicable for FSO links. High quality lasers and detectors are readily available. These wavelengths are also used in the fibre technology. As radiation sources, Fabry-Perot and *Distributed-Feedback lasers* (DFB) based on InGaAs/InP semiconductor technology are used. For construction of an FSO receiver, InGaAs detectors are usually applied. These detectors based on PIN or APD technology are optimized for operation at the wavelength of 1310 nm or 1550 nm providing a data rate of 10 Gbps.

The *long-wavelength-infrared spectrum* (LWIR) FSO systems are more challenging because of practical aspects. However, in this spectral range, there is observed a smaller impact of absorption and scattering on beam propagation through moderate fog comparing with that of other infrared ranges. Also, atmospheric turbulence is characterized by a smaller impact on transmission. Additionally, a smaller influence of solar radiation (29 dB) at a wavelength of 10 μm, comparing with the wavelength of 1550 nm is noticed [36, 37]. Recently developed *quantum cascade lasers* (QCL) are very attractive radiation sources operating in this spectral range. They are compact, high-power semiconductor lasers with the frequency characteristics of even 100 GHz bandwidth. This makes QCLs important tools for constructing communication systems. In the case of FSO receiver design, an MCT detector characterized by ultra-high detectivity and GHz signal bandwidth is applied.

Summarizing, there are three different optical radiation spectra employed in FSO systems. In their construction, different radiation sources and detectors are used. These optoelectronic elements are characterized by parameters dependent on wavelengths and data rates. That is why the analyses of FSO system design should take into consideration the impact of the operation spectra on the atmosphere transmission. For example, Fig. 8a shows the total attenuation versus low visibility at wavelengths of 780 nm, 850 nm and 1550 nm. These wavelengths correspond to the operation spectral ranges of commercially available FSO systems. The total attenuation at a wavelength of 1550 nm is lower than at others. Therefore, to reduce the beam attenuation during hazy days, the SWIR-FSO system should be used. It is observed that the radiation attenuation increases with the link range (Fig. 8b). For a radiation wavelength of 1550 nm, the growth speed is lower than for others.

The performed analyses show that the atmospheric attenuation depends also on the rainfall rate (Fig. 9). However, rain has not so strong spectral influence, because raindrops have larger size compared with laser wavelengths causing minimal scattering of light beam.

Nowadays, the dynamic development of LWIR-FSO systems is observed. But these works are mainly performed at lab-experiment level. In Fig. 10 a comparison of LWIR radiation

attenuation with that obtained for other ranges for different values of visibility is presented. It is shown that the LWIR range is characterized by better transmission in a wide range of visibility.

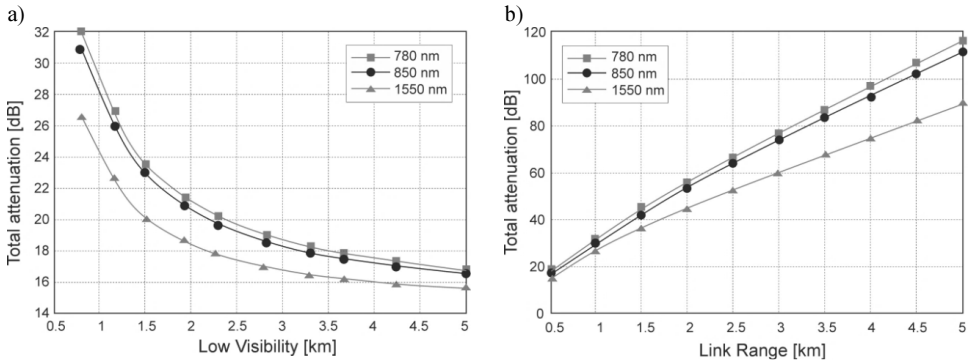

Fig. 8. Total attenuation versus average visibility (a); and total attenuation versus link range for different wavelengths (b).

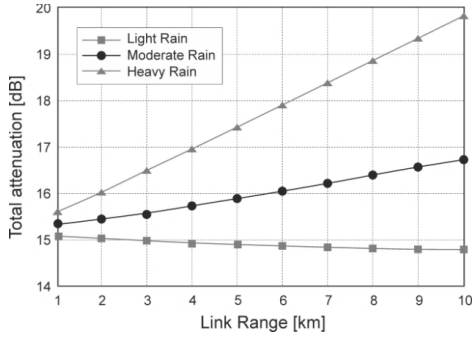

Fig. 9. Total attenuation versus link range for different rainfall rates.

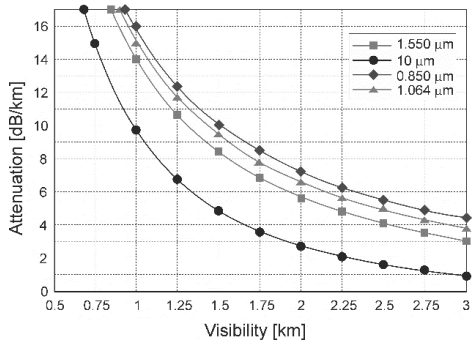

Fig. 10. Radiation attenuation versus visibility [38].

There are only a few reports describing results of experimental verification of beam transmission at the wavelengths of interest. Fig. 11a shows transmission losses for four different wavelength links as a function of time.

There was observed a significant decrease in transmission for three shorter wavelengths during the day time. In the same time, an increase of water vapour concentration was also registered. Similar experiments were performed for different oil vapour concentrations. In this situation, the LWIR radiation is also characterized by the lowest attenuation (Fig. 11b).

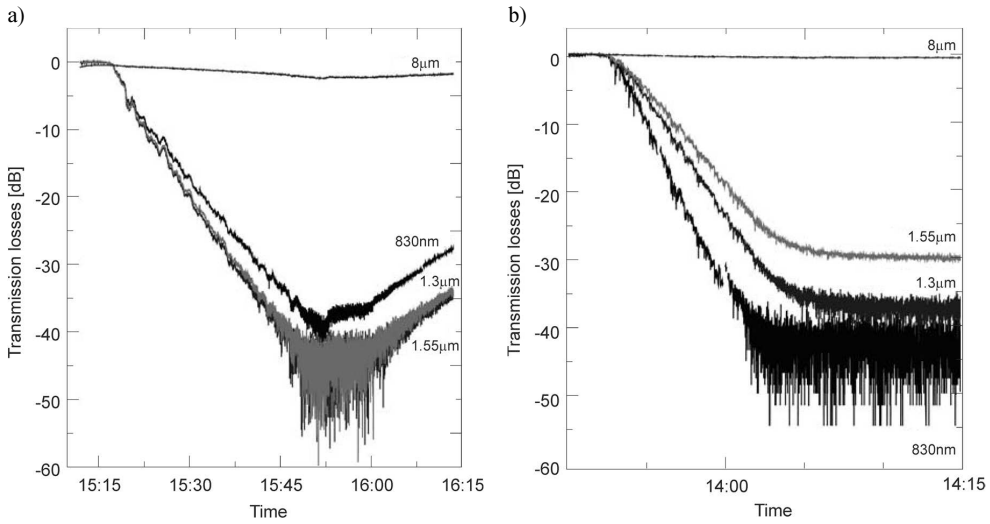

Fig. 11. Transmission losses for four different wavelengths of FSO links: as a function of time during which the water vapour concentration increased (a); as a function of increased oil vapour concentration (b) [39].

6. FSO/RF hybrid data link

Free Space Optics is sensitive to atmospheric conditions reducing visibility, *e.g.* precipitation, fog, haze, or scintillation. These factors may limit the data link range to a few km or several hundred metres. It is also known that RF links show good transmission in fog, but high attenuation in the presence of precipitations like rain and snow. This results in a better matching the RF wavelength to sizes of *e.g.* rain droplets. However, RF channels are also more susceptible to interference and jamming.

Combining these two technologies into one FSO/RF hybrid link may increase the data transfer availability and ensure higher security keeping a high speed of transmission. Such a hybrid construction can be classified into three categories: redundant systems, switch-over systems and load-balancing systems [40]. The redundant systems duplicate data and transmit them simultaneously over both the FSO and RF data links. In contrast, the switch-over systems transmit data using only one link. Usually, the FSO link is chosen as the primary link whereas the RF one operates as a backup. In practice, the RF link compensates the reduced bandwidth of FSO link during bad-weather conditions. The load-balancing systems distribute the data traffic between the FSO and RF links according to the connectivity quality, thus exploiting the full available bandwidth at each time.

The hybrid FSO/RF technology is especially dedicated to military communication systems, crisis management, intelligent transportation systems, and telemetry. In the military area, it can be used in transmission systems at Tactical Operations Centres, airborne networks, cross-links between satellites, as well as in different types of platforms: space-to-air, space-to ground and air-to-ground [41].

7. Free Space Optics technology at the Institute of Optoelectronics, MUT

In the Institute of Optoelectronics, the research related to laser communication systems started in 1990s. The first FSO system operating at a wavelength of 850 nm was developed in 1993 and provided a data transfer rate of 10 kbps. In 2004, there was constructed the second system with a transfer rate of 100 Mbps and an operation wavelength of 1.54 μm. The work on LWIR-FSO links was started in 2006. That link used QCL's laser system from Cascade Technologies. The receiver consisted of an off-axis mirror system from Janes Technology and a low-noise MCT detection module from VIGO System S.A. The main limiting factors of its data transmission rate were the modulation bandwidth and the duty cycle of generated pulses.

Thanks to the recent progress in semiconductor technology, QC lasers with a much higher power, repetition rate and duty cycle of pulses have been constructed. In 2009, it was decided to design the second model of LWIR FSO link. In that construction, a laser system of Alpes Lasers SA, a germane lens and optimized MCT detection modules from VIGO System S.A were used. To connect the optical link with the data network, a fully programmable RCM 4200 module operated by a Rabbit 4000 processor with a complete Ethernet interface was applied. The module worked as a buffer for receiving data frames from Ethernet network, performing data analysing and validation. Parameters of the two LWIR-FSO systems are listed in Table 2.

Table 2. Parameters of the constructed LWIR-FSO data links.

Parameter	First model (2006)	Second model (2009)
Operation wavelength	10 μm	8.4 μm
Pulse peak power	100 mW	200 mW
Detection module detectivity	$3.2 \cdot 10^9$ cmHz$^{1/2}$/W	$3 \cdot 10^{10}$ cmHz$^{1/2}$/W
Beam divergence	1.5mrad	2.5 mrad
Data rate	115 kbps	2 Mbps
Range	1.5 km (Vis = 2 km)	2.5 km (Vis = 2 km)

8. LasBITer Project of radio-optical data link

LasBITer is a hybrid data link design consisting of optical and radio communication channels (Fig. 12). The FSO transmitter project consists of a compact laser head with a QC laser constructed at the Institute of Electron Technology, a laser driving unit, a temperature controller and a parabolic off-axis mirror optical device. Additionally, the device is equipped with a laser power monitoring system.

8.1. Project description

The FSO receiver is built of an optimized optical system and a detection module from VIGO System S.A. The optical system provides both high data rate and good conditions to start the FSO data link and to minimize the influence of turbulence on the link availability. The detection module is equipped with an MCT detector and a pulse power control unit.

The communication unit enables data transmission using the designed FSO system and a commercial RF. It also enables measuring a bit error rate in each of these channels. It is based on XILINX FPGAs technology. This application enables flexible changing of both data coding and configuration of forward error correction methods. In this unit, a control data stream is added to the useful information in order to monitor the link quality.

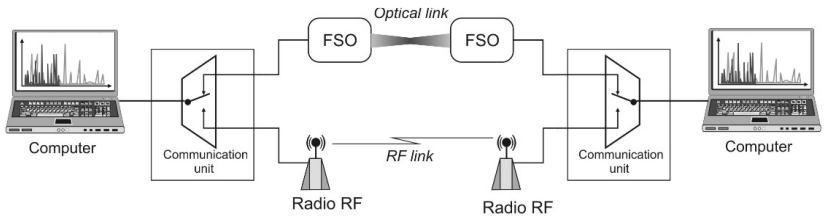

Fig. 12. A concept of the FSO/RF hybrid data link.

A special controller of FSO data link is also developed to control the parameters of its key-components (power supplies, radiation power, operation temperature, *etc*.). The radio data link is based on commercial transmission modules operating at the military frequency of 1.4 GHz. Two modes of co-operation of FSO-LWIR and RF are designed. In the independent operation mode, the data link user decides which of the channels will be used for data transmission. It is also possible to distribute the data proportionally to the configured data rate, so-called load balancing, using the second mode of its operation.

Compared with some previously reported hybrid systems [42, 43], the *LasBITer* data link design has a better data range, communication availability, and transfer data safety.

The goals should be obtained by the use of dedicated 8÷12 μm quantum cascade lasers and optimized MCT detection modules.

8.2. Quantum cascade lasers

The quantum cascade lasers are unipolar devices based on tunnelling and inter-sub-band transitions, in which the electronic states, wave functions and lifetimes of relevant states are engineered through the quantum mechanical confinement imposed by a complex multilayer structure. The second main feature of this type of lasers is the cascading scheme of carriers' route through the laser active region. That means that a single carrier is used more than one time for generating a photon carrier. For QCLs operation, an extremely precise tailoring of energy levels of quantum states, optical dipole matrix elements, tunnelling times and scattering rates of carriers is required. The physical basis of QCLs operation is fundamentally different from that of classical bipolar semiconductor lasers, in which the emission is due to the inter-band radiative recombination of pairs of carriers instead of inter-sub-band transitions which lead to lasing in QCLs [44].

At this moment, a wavelength range of QCL radiation spans from ~3.5 μm up to ~250 μm. So it generally covers a very wide infrared spectrum, from mid-IR up to far-IR. In comparison with the performance of bipolar lasers, this one provides about two orders of magnitude increase of the wavelength range available for semiconductor lasers, towards the longer wavelengths. The huge spectral flexibility of the emission is a result of the application of the intra-band generation mechanism.

For the purpose of *LasBITer* data link project, the lattice matched (~9.2÷9.4 μm) $Al_{0.48}In_{0.52}As/In_{0.53}Ga_{0.47}As/InP$ QCLs technology has been selected [45, 46]. The laser structures consisted of 30- segments. The active region of the lasers was of a 4-well 2-phonon resonance design. The layer sequence of one period of the structure, in nanometres, starting from the injection barrier is: **4.0**, 1.9, **0.7**, 5.8, **0.9**, 5.7, **0.9**, 5.0, **2.2**, 3.4, **1.4**, 3.3, **1.3**, 3.2, **1.5**, 3.1, **1.9,** 3.0, **2.3**, 2.9, **2.5, 2.9** nm. The AlInAs layers are printed in bold. The total thickness of one period is 59.8 nm. The underlined layers are *n* doped to $2.0 \times 10^{11}cm^{-2}$. The conduction band profile and squared wave-functions of moduli in the injector/active/injector segment of the $Al_{0.48}In_{0.52}As/In_{0.53}Ga_{0.47}As/InP$ laser under the applied field of 50 kV/cm are shown in Fig. 13.

The electronic band structure of QCL has been calculated by solving the Schrödinger equation with position-dependent effective mass.

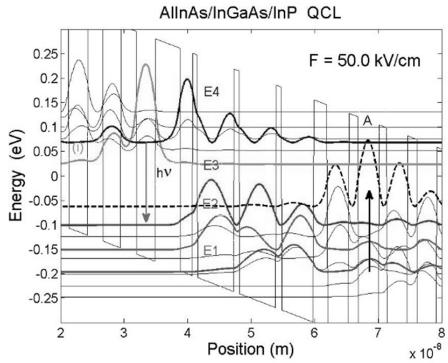

Fig. 13. The conduction band profile and squared wave-functions of moduli in the injector/active/injector segment of the laser under the applied field F = 50 kV/cm (at threshold). The wave-functions have been shifted to the energy positions of the respective levels. E4, E3, E2 and E1 refer to the upper, lower and ground states of lasing transitions. The black dashed line denotes the "spurious" excited state in the injector mini-gap. The lowest energy state in the injector couples directly to the upper laser level E4 [45].

The active region of the laser is embedded in the waveguide formed from the lower side by a low-doped InP substrate and from the upper side by a 2.5 μm AlInAs layer. The layer structure of AlInAs/InGaAs/InP laser is shown in Table 3. The whole laser structure was grown by MBE.

Table 3. A layer structure of AlInAs/InGaAs/InP lasers.

500 nm	InGaAs	n = 8e18 cm^{-3}	
2.5 μm	AlInAs	n = 1e17 cm^{-3}	Upper Waveguide
500 nm	InGaAs	n = 4e16 cm^{-3}	
~1.8 μm	**30 x AlInAs/InGaAs**		Active Region
500 nm	InGaAs	n = 4e16 cm^{-3}	Lower Waveguide
500 μm Substrate	InP	n = 2e17 cm^{-3}	

The lasers work at up to 340 K (~60ºC), emitting tens of mW of pulse power. At 20ºC the optical power per uncoated facet is of the order of 0.6 W. The slope efficiency is up to 1 W/A at room temperature; the wall plug efficiency is ~4%. The room-temperature light-current and current-voltage characteristics of the laser emitted at 9.2 μm are shown in Fig. 14.

The laser parameters can be further improved by optimizing the waveguide design, *i.e.*, by employing a symmetric InP waveguide. In this case, a conductive substrate can be used to grow the lower waveguide by MOVPE, then the active region is grown by MBE, and finally the upper waveguide is completed by MOVPE. That complicates technology, however a clear advantage, despite the increase of confinement factor, is the suppression of the free carrier absorption in the lower waveguide and consequent lowering of the threshold current. The parameters of developed devices are summarized in Table 4.

The lasers with a symmetric InP waveguide, due to a lower threshold current, should enable obtaining higher output powers which is advantageous in optical communication systems. Additionally, when processed into a buried active region type device, they can be CW-operated.

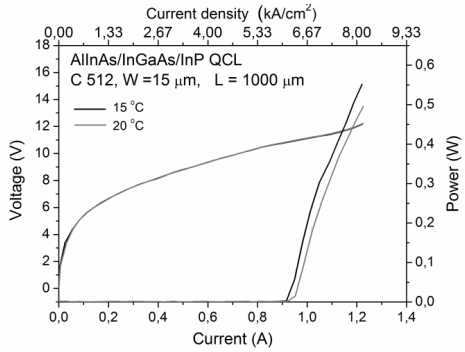

Fig. 14. Light-current and current-voltage characteristics of the Al0.48In0.52As/In0.53Ga0.47As/InP (λ = 9.2 μm) laser driven by 200 ns pulses with a repetition rate of 1 kHz [45].

Table 4. Parameters of AlInAs/InGaAs/InP lasers.

Parameter	Symbol	Value
Threshold current density	J_{th}(77 K)	2 kA/cm^2 – 3 kA/cm^2
	J_{th}(300 K)	~5 kA/cm^2
Threshold voltage	V_{th}(77 K)	10 V
	V_{th}(300 K)	11 V
Peak power (per facet)	P (77 K)	~2 W
	P (300 K)	~0.6 W
Max operating temperature	T_{max}	340 K
Characteristic temperature	T_0 (K)	120 K – 140 K
Differential gain	gΓ (77 K)	(5.7–6) cm^{-1}/kA
	gΓ (250 K)	(1.9–2.5) cm^{-1}/kA
Waveguide losses	α_w (77–300) K	~18 cm^{-1}
Wall-Plug efficiency	WPE	~4 %
Slope efficiency	η_{ext}	~1 W/A

8.3. MCT detection modules

VIGO System S.A. produces unique infrared detection modules (Fig. 15) that integrate in common packages infrared photodetectors, Peltier coolers, signal processing electronics, heat dissipation systems and other components [47]. The integration makes the detectors less vulnerable to electromagnetic interferences, over-bias, electrostatic discharges, and other environmental exposures. Additional advantages of the integration are: improved HF performance, standardization of the output signal, miniaturization and cost reduction.

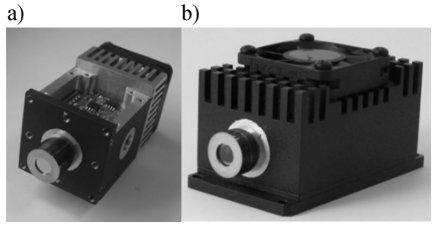

Fig. 15. Detection modules with a photodiode: unbiased (a) and biased (b).

The photodetector submodule (Fig. 16) consists of an optically immersed LWIR (~10 μm) hetero-structure photodiode, a 4-stage Peltier cooler and a temperature sensor housed in a hermetically sealed TO-8-based package, designed for detector operation at a temperature of approx. 200 K. The package is evacuated and then backfilled with a krypton/xenon mixture. It is supplied in optically transparent windows, absorbers of residual active gases (H_2O, O_2 and CO_2), convection and cold shields.

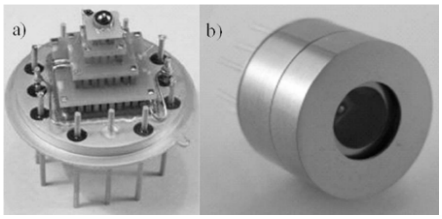

Fig. 16. An optically immersed detector mounted on a four-stage Peltier cooler (a) and a TO-8 header-based detector housing (b).

The photodiode construction is based on a modified HgCdTe PIN hetero-structure, grown by Metal Organic Vapor Phase Epitaxy [48–51]. Its architecture has been optimized by numerical simulation using a commercially available APSYS software package. The photodiode design is aimed to achieve fast and efficient collection of charge carriers, a low electric capacitance (of both depletion and diffusion layers) and a low series resistance [52].

The use of monolithic optical immersion of active elements in a high refraction index hyper-hemispherical lens results in a dramatic improvement of performance compared with the non-immersed device of the same optical size, namely a decrease of electric capacitance and dark current by two orders of magnitude [53]. In addition, the use of the double pass of radiation for enhanced absorption makes possible the reduction of the absorber thickness keeping unchanged the quantum efficiency.

A measured current-voltage plot of the photodiode (Fig. 17) shows three different bias ranges. The dark current initially increases with the reverse bias voltage, saturating in a range from −60 mV to −100 mV and then increases at higher voltages. A more close analysis reveals the diffusion nature of the dark current at low bias with a significant influence of series resistance at weak reverse bias. The dark current in the saturation range is mostly due to the Auger 7 and Shockley-Read-Hall thermal generation. The increase of dark current at a biasing voltage higher than −200 mV is due to the tunnel current, reduced to some degree by the series resistance.

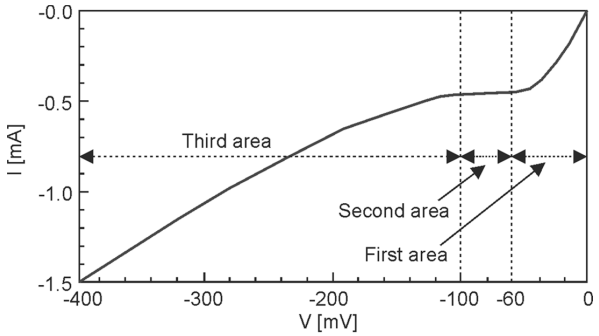

Fig. 17. A reverse dark current-voltage plot measured at 200 K. The background radiation was suppressed by 200 K cold shield. A physical photodiode area is $0.03 \times 0.03 mm^2$.

Figure 18 shows a block diagram of the module electronic circuitry. The electronic circuitry provides optimized conditions for the photodiode operation – a constant voltage bias and a readout of current mode. The first stage is a DC-coupled trans-impedance preamplifier of a low input resistance, based on OPA 847 opamp, characterized by a low input noise voltage (0.85 nV/Hz$^{1/2}$) and a moderate input noise current (2.5 pA/Hz$^{1/2}$). The second stage is a ~20 dB AC-coupled voltage preamplifier with a 50 Ω output resistance, rejecting the DC phodiode signal component.

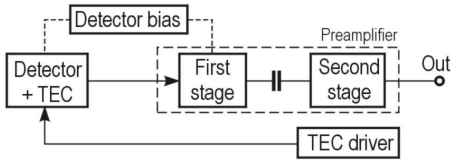

Fig. 18. A block diagram of the detection module.

A Peltier cooler driver has been used to keep temperature constant with accuracy better than 0.1ºC, at ambient temperatures of up to 50ºC. The heat generated inside the module by the Peltier cooler and the signal processing circuitry is dissipated with miniaturized fans.

Spectral responses of the detection modules have been measured using blackbody calibrated Fourier Transform Spectrophotometers. The module output noise voltage was determined with a signal analyser. Spectral detectivity was calculated as the signal-to-noise ratio, normalized to 1 cm^2 detector optical area and 1 Hz bandwidth (Fig. 19). The observed increase of detectivity with bias is mostly due to the elimination of recombination noise of the photodiode and the increased ratio of the series-to-parallel diode resistances, resulting in a significant increase of the current responsivity. It should be noted, that detectivity decreases at low (<~ 100 kHz) frequencies due to 1/*f* noise of the biased photodiodes. In contrast, the unbiased photodiodes are practically 1/*f* noise-free, similarly to other optical detectors [54].

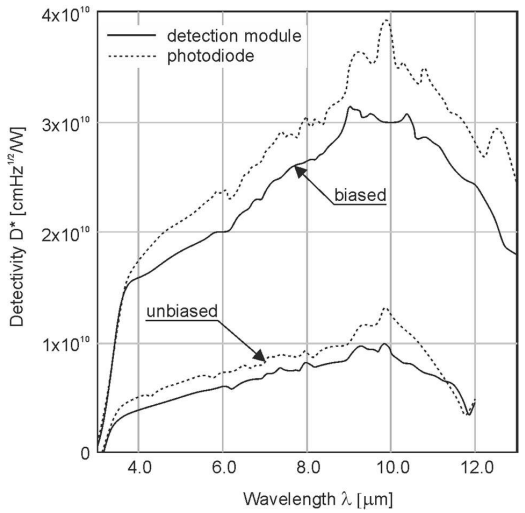

Fig. 19. The spectral detectivities of the photodiodes operating at zero and 200 mV bias measured for the detection module and for the photodiode itself (with subtracted preamplifier noise).

A frequency response of the modules was measured using an optical parameter oscillator generating ~25 ps pulses of 10 µm infrared radiation. A signal decay time constant was measured by an 8 GHz bandwidth oscilloscope. Table 5 shows basic parameters of the two modules, with unbiased and 0.2 V biased ~10 µm photodiodes, respectively.

Table 5. Basic parameters of the detection modules.

Parameter	Unit	Module 1	Module 2
Photodiode area	mm	0.3 × 0.3	0.3 × 0.3
Photodiode temperature	K	200	200
Bias voltage	V	0	-0.2
Transimpedance @ R_{LOAD} = 50 Ω	V/A	$27 \cdot 10^3$	$13.5 \cdot 10^3$
Output resistance	Ω	1000	50
Gain bandwidth	MHz	0.001÷150	0.001÷1000
Noise voltage	$nV/Hz^{1/2}$	430	210
Voltage responsivity @ 10 µm	V/W	130000	210000
Detectivity @ 10 µm	$cmHz^{1/2}/W$	$9 \cdot 10^9$	$3 \cdot 10^{10}$
Time constant	ns	4.0	0.26

Basing on the measurement data it can be seen that the reverse biased modules could achieve detectivity smaller by a factor ~2 than the fundamental 300 K BLIP limit of performance (FOV = 180°). At present, intensive research is under way on miniaturized modules for >1 GHz bandwidth with detector and electronic blocks hermetically sealed in miniaturized packages (Fig. 20).

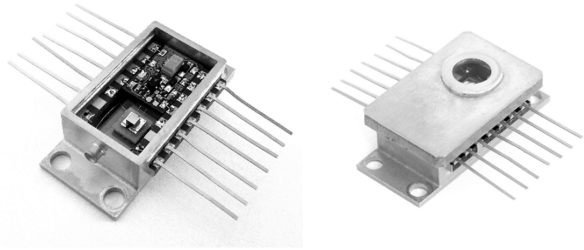

Fig. 20. Miniaturized detection modules before and after sealing.

9. Summary

The described analysis presents a high potential of FSO technology in the development of wireless mobile communication systems. The properties of FSO systems can be defined by both transmitter and receiver parameters. However, the greatest limitation of these systems is directly determined by the influence of the atmosphere. In this case, minimizing this negative effect mainly depends on the wavelength range of FSO link operation. The research performed so far has shown that a very promising solution may be the use of transceivers operating in the LWIR spectrum. This spectrum corresponds to the atmospheric transmission window while

being less affected by scattering and scintillation in comparison with existing NIR- or SWIR-FSO systems.

To further increase the availability of wireless communications, so-called hybrid links can be used. These constructions use both optical and radio communication channels. The preliminary research on this type of devices is currently underway. These studies are also the primary task of the described LasBITer project. In this project, a unique combination of free-space optical and radio links is used. The essential elements of the FSO link are quantum cascade lasers and MCT integrated detection modules. These lasers can be potentially used in other applications as well (*e.g.* Raman spectroscopy at different excitation wavelengths for advance chemical compounds detection [55]). The described processes of these devices' design have resulted in obtaining the optimal time-energy parameters of generated pulses, as well as the ability to detect ultra-low power LWIR radiation pulses .

Acknowledgements

This research was supported by The Polish National Centre for Research and Development grant DOB-BIO8/01/01/2016.

Refernces

[1] Taslakov, M.A., Simeonov, *et al.* (2004). Quantum cascade laser based system for line-of-sight data transmission in the mid IR. *Proc. SPIE 5830*, doi:10.1117/12.618774.

[2] Uysal, M., *et al.* (2016). Optical Wireless Communications An Emerging Technology. Signals and Communication Technology, 1–23.

[3] Saini, S., Gupta, A. (2014). Investigation to Find Optimal Modulation Format for Low Power Inter-Satellite Optical Wireless Communication. *Wireless and Optical Communications Networks (WOCN)*, doi: 10.1109/WOCN.2014.6923094.

[4] Alkholidi, A.G., Altowij, K. (2012). Optical Communications Systems: Effect of clear atmospheric turbulence on quality of free space optical communications in Western Asia. *InTECH*, doi 10.5772/1807.

[5] Fletcher, G.D.T., Hicks, R., Laurent, B. (2002). The SILEX optical interorbit link experiment. *IEEE J. Elec. & Comm. Eng.*, 3(6), 273–279.

[6] Muth, J. (2017). *Free-space Optical Communications: Building a 'deeper' understanding of underwater optical communications*. Laser Focus World.

[7] Wilson, K.E., Lesh, J.R. (1993). An overview of galileo optical experiment (GOPEX), Tech Report: TDA progress Report 42–114. *Communication Systems Research Section*, NASA.

[8] Wilson, K.E. (1996). An overview of the GOLD experiment between the ETS-VI satellite and the table mountain facility, TDA Progress Report 42–124. *Comm. Sys. and Research Sec.*, 9–19.

[9] Chlestil, Ch., *et al.* (2007). Optical wireless on swarm UAVs for high bit rate application. *The Mediterranean Journal of Computers and Networks*, 3(4), 142–150.

[10] Ortiz, G.G., *et al*. (2003). Design and development of a robust ATP subsystem for the altair UAV-to-ground lasercomm 2.5-Gbps demonstration. *Proc. SPIE 4975*, 103–114.

[11] *http://www.cyberbajt.pl/raport/40/0/142/*

[12] Wang, Ch.Y., *et al.* (2009). Mode-locked pulses from mid-infrared Quantum Cascade Lasers. *Optics Express*, 17(15), 12929–12943.

[13] Catalogue of Sonardyne firm (2017). Sonardyne Subsee Technology.

[14] Sadiku, M.N.O., *et al.* (2016). Free Space Optical Communications: An Overview. *European Scientific Journal*, 12(9).

[15] Kazaura, K., *et al.* (2008). Studies on next generation access technology using radio over free space optic links. *2nd International Conference on Next Generation Mobile Applications, Services, and Technologies – presentation*.

[16] Ramirez-Iniguez, R., Idrus, S.M., Sun, Z. (2007). *Optical Wireless Communications IR for Wireless Connectivity*. Taylor & Francis Group, CRC Press.

[17] Arnon, S. (2003). Optical Wireless Communications. *Encyclopedia of Optical Engineering.*

[18] Kasap, S., Ruda, H., Boucher, Y. (2009). *Cambridge illustrated handbook of optoelectronics and photonics*. Cambridge University Press.

[19] Bouchet, O., *et al*. (2010). *Free-Space Optics: Propagation and Communication*. Book, Wiley-ISTE.

[20] Talib, M.F., *et al.* (2017). Investigation on heavy precipitation effects over FSO link. *MATEC Web of Conferences*, 97, 01113 doi: 10.1051/matecconf/20179701113.

[21] Stull, R.B. (1988). *Atmospheric Sciences Library: An Introduction to Boundary Layer Meteorology*. Kluwer Academic Publishers.

[22] Alkholidi, A.G., Altowij, K.S. (2014). *Free Space Optical Communications –Theory and Practices.*

[23] Lawson, J.K., Carrano, C.J. (2006). Using Historic Models of Cn2 to predict r0 and regimes affected by atmospheric turbulence for horizontal, slant and topological paths. *Proc. SPIE 6303*, doi:10.1117/12.679108.

[24] Bloom, S. (2001). The physics of free-space optics. *AirFiber Inc*., 802-006-000, M-A1, 1–22.

[25] Singal, P., Rai, S., Punia, R., *et al*. (2015). Comparison of different transmitters using 1550 nm and 10 000 nm in FSO communication systems. *Int. Journal of Computer Science & Information Technology*, 7(3), 107–112.

[26] Berman, G.P., Chumak, A.A., *et al.* (2007). Beam wandering in the atmosphere: the effect of partial coherence. *Physical Review E*, 76, 056606-1–056606-7.

[27] Xian, Q., Wen-Yue, Z., *et al*. (2012). Long-distance propagation of pseudo-partially coherent Gaussian Schell-model beams in atmospheric turbulence. *Chin. Phys. B*, 2(9), 094202-1–094202-8.

[28] Zaki Rashed, A.N., Sharshar, H.A. (2014). Error Probability and Laser Beam Propagation Analysis in Local Area Optical Wireless Communication Networks Using Pulse Position Modulation Technique under Atmospheric Turbulence Effects. *International Journal of Advanced Research in Electronics and Communication Engineering (IJARECE)*, 3, 261–272.

[29] Willebrand, H., Ghuman, B. (2002). *Free Space Optics: Enabling Optical Connectivity in Today's Networks*. Sams Publishing.

[30] Bloom, S., Korevaar, E., *et al*. (2003). Understanding the performance of free-space optics. *Journal of Optical Networking*, 2(6), 178–200.

[31] Rongqing, H., O'Sullivan, M. (2009). *Fiber Optic Measurement Techniques*, 486–494.

[32] Forin, D.M., Incerti, G. (2010). Free Space Optical Technologies: *Trends in Telecommunications Technologies*, ed. Bouras, Ch.J.

[33] Altowij, K.S., Alkholidi, *et al*. (2010). The effect of Clear Atmospheric Turbulence on the Quality of the Free Space Optical Communications in Yemen. *Frontiers of Optoelectronics in China*, 3(4).

[34] Boone, B.G., Bruzzi, J.R., *et al*. (2004). Optical Communications Development for Spacecraft Applications. *Johns Hopkins Apl Technical Digest*, 25(4), 306–315.

[35] IEC 60825-1, International Standard, Safety of laser products, Edition 3.0 2014-05.

[36] Manor, H., Arnon, S. (2003). Performance of an optical wireless communication system as a function of wavelength. *Applied Optics*, 42(21), 4285–4294.

[37] Pavelchek, A., Trissel, R., *et al*. (2004). Long wave infrared (10 μm) Free Space Optical Communication. *Proc. of SPIE*, 5160, 247–252.

[38] Soni, G., Malhotra, J.T. (2011). Free Space Optics System: Performance and link availability. *International Journal of Computing and Corporate Research*, 1(4).

[39] Martini, R., Whittaker, E.A. (2005). Quantum cascade laser-based free space optical communications. *J. Opt. Fiber. Commun. Rep*., 2, 1–14.

[40] Leitgeb, E., Plank, T., *et al*. (2014). Free Space Optics in different (civil and military) application scenarios in combination with other wireless technologies. *Telecommunications Network Strategy and Planning Symposium (Networks)*, doi: 10.1109/NETWKS.2014.6959207.

[41] Milner, S.D., Davis, C.C. (2004). Hybrid free space optical/RF networks for tactical operations. *Military Communications Conference (MILCOM)*, doi: 10.1109/MILCOM.2004.1493303.

[42] Akbulut. A., *et al.* An experimental hybrid FSO/RF communication system. Research supported by Ankara University Scientific Research Projects, Project No: 2001-00-00-006.

[43] Nadeem, F. *et al.* (2009). Weather effects on hybrid FSO/RF communication link. *IEEE Journal on Selected Areas in Communications,* 27(9).

[44] Faist, J. (2013). *Quantum cascade lasers*. Oxford University Press.

[45] Gutowski, P., Karbownik, P., *et al.* (2014). Room Temperature AlInAs/InGaAs/InP Quantum Cascade Lasers. *Photonics Letters of Poland*, 6(4), 142–144.

[46] Gutowski, P., Sankowska, I., *et al.* (2017). MBE Growth of Strain-Compensated InGaAs/InAlAs/InP Quantum Cascade Lasers. *Journal of Crystal Growth*, 466, 22–29.

[47] Gutowska, M., Gawron, W., *et al.* (2010). New Detection Modules for Free Space Optics. *Photonics Letters of Poland*, 2(2).

[48] Piotrowski, J., Orman, Z., *et al.* (2005). Uncooled long wave infrared photodetectors with optimized spectral response at selected spectral ranges. *Proc. SPIE*, 5783.

[49] Piotrowski, A., Gawron, W., *et al.* (2005). Improvements in MOCVD growth of Hg1-xCdxTe heterostructures for uncooled infrared photodetectors. *Proc. SPIE*, 5957, 108–116.

[50] Piotrowski, A., Klos, K., *et al.* (2007). Uncooled or minimally cooled 10μm photodetectors with subnanosecond response time. *Proc. SPIE*, 6542.

[51] Piotrowski, J., Rogalski, A. (2007). *High-Operating-Temperature Infrared Photodetectors*. SPIE.

[52] Piotrowski, J., Piotrowski, A. (2010). *Mercury Cadmium Telluride: Growth, Properties and Applications: Room temperature photodetectors*. ed. Capper, P., Garland, J., Willey.

[53] Piotrowski, J., Galus, W., *et al.* (1991). Near Room-Temperature IR Photo-detectors. *Infrared Phys*., 31, 11–48.

[54] Gnyba, M., Smulko, J., Kwiatkowski, A., Wierzba, P. (2011). Portable Raman spectrometer-design rules and applications. *Bulletin of the Polish Academy of Sciences: Technical Sciences*, 59(3), 325–329.

[55] Kwiatkowski, A., Czerwicka, M., Smulko, J., Stepnowski, P. (2014). Detection of denatonium benzoate (Bitrex) remnants in noncommercial alcoholic beverages by raman spectroscopy. *Journal of Forensic Sciences*, 59(5), 1358–1363.